Available online at www.sciencedirect.com
SCIENCE DIRECT®
Journal of Power Sources 125 (2004) 40–51
JOURNAL OF POWER SOURCES
www.elsevier.com/locate/jpowsour

Three-dimensional analysis of transport and electrochemical reactions in polymer electrolyte fuel cells

Sukkee Um, C.Y. Wang*

Department of Mechanical and Nuclear Engineering, Electrochemical Engine Center, The Pennsylvania State University, 338 Reber Building, University Park, PA 16802, USA

Received 21 June 2003; accepted 12 July 2003

Abstract

A computational fuel cell dynamics (CFCD) model is presented to elucidate three-dimensional (3D) interactions between mass transport and electrochemical kinetics in polymer electrolyte fuel cells with straight and interdigitated flowfields, respectively. The model features a detailed membrane–electrode assembly (MEA) submodel in which water transport through the membrane with spatially variable transport properties and spatial variations of the reaction rate and ionic resistance through the catalyst layer are accounted for. Emphasis is placed on obtaining a basic understanding of how three-dimensional flow and transport phenomena in the air cathode impact the electrochemical process in both types of the flowfield. Fully three-dimensional results of the flow structure, species profiles and current distribution are presented for proton exchange membrane (PEM) fuel cells with an interdigitated cathode flowfield. The model results indicate that forced convection induced by the interdigitated flowfield substantially improves mass transport of oxygen to, and water removal from, the catalyst layer, thus leading to a higher mass-transport limiting current density as compared to that of the straight flowfield.

Keywords: Polymer electrolyte fuel cells; Interdigitated flowfield; Modeling and simulation

1. Introduction

Approaching the limiting current density, cell polarization results mainly from the limit of oxygen transport through the air cathode in proton exchange membrane (PEM) fuel cells. The near-zero oxygen concentration at the cathode gas-diffuser/catalyst–layer interface occurs due to the lower oxygen diffusivity (three to four times lower) than the hydrogen diffusivity. When pure oxygen is used instead of air, this mass-transport limitation can be relaxed. Alternatively, innovative flowfield designs such as the interdigitated cathode are required to enhance mass transport through the gas-diffusion layer (GDL) underneath the current collector and assist oxygen reduction reaction (ORR) within the cathode reaction zone, resulting in improved cell performance.

In the previous model of Um et al. [1], a computational fuel cell dynamics (CFCD) model was used to understand the electrochemical and transport phenomena of PEM fuel cells in the two-dimensional (2D) situation. In particular, the oxygen transport limitation in the through-plane direction from the gas channel across the GDL to the catalyst layer as well as along the flow channel direction was fully discussed. In a real PEM fuel cell geometry, there exists, however, the mass-transport limitation in the third dimension, namely along the catalyst layer from the channel to under the current-collecting rib. This is so-called rib effect. As a result, the average cell current density in the three-dimensional geometry is always lower than the two-dimensional prediction in which the mass-transport limitation is absent in the third direction.

Building upon the model from the preceding work of Um et al. [1], the present work is focused on studying the mass-transport limitation between the channel and landing area over a length scale of approximately one millimeter, and the associated rib effect. In addition, the inclusion of the third dimension brings about an innovative flowfield design, called interdigitated flow. In the conventional straight flowfield, gas flows along the surface of GDL, thereby leading to oxygen transport controlled predominantly by molecular diffusion through the GDL, but in the interdigitated flowfield as schematically shown in Fig. 1, two flow channels around each current-collector shoulder have a dead-end, so the reactant gas is forced to flow through the porous GDL in order to exit. This forced convection mechanism facilitates

* Corresponding author. Tel.: +1-814-863-4762; fax: +1-814-863-4848.
E-mail address: cxw31@psu.edu (C.Y. Wang).

0378-7753/$ – see front matter © 2003 Elsevier B.V. All rights reserved.
doi:10.1016/j.jpowsour.2003.07.007

Nomenclature

a	effective catalyst area per unit volume (cm^2/cm^3)
A	electrode geometrical area (cm^2)
c	molar concentration (mol/cm^3)
D	mass diffusivity of species (cm^2/s)
F	Faraday constant (97487 C/mol)
H	gas channel height (cm)
I	current density (A/cm^2)
j	transfer current (A/cm^3)
K	hydraulic permeability (cm^2)
L	cell length (cm)
n_d	electro-osmotic drag coefficient
P	pressure (Pa)
R	gas constant (8.314 J/mol K)
RH	relative humidity
S	source term in transport equations/ current-collector thickness
t	time (s)
T	temperature (K)
$\vec{u}$	velocity vector (cm/s)
U	inlet velocity calculated by Eqs. (1) and (2) (cm/s)
V	cell potential (V)
x, y, z	cell coordinates
X	mole fraction

Greek letters

α	transfer coefficient
ϵ	porosity
Φ	phase potential (V)
ϑ	volumetric flow rate (cm^3/s)
κ	ionic conductivity (S/m)
μ	viscosity (kg/m s)
ρ	density (kg/cm^3)
ζ	stoichiometry

Superscripts

c	cathode
eff	effective value
m	membrane phase
sat	saturation value

Subscripts

a	anode
c	cathode
cell	fuel cell
e	electrolyte
in	inlet
k	species
oc	open circuit
ref	reference value
u	momentum equation
Φ	potential equation

transport of reactants to, and products from, the catalytic reaction layer, thus increasing the current density at a given cell potential.

Experimental studies have demonstrated the effectiveness of the interdigitated flowfield [2–5]. However, the complex flow structure induced by the interdigitated flowfield and its impact on the transport and electrochemical processes remain to be delineated. Several attempts [6,7] have been made to develop two-dimensional mathematical models for the problem, but the 2D models are limited in their ability to capture the highly three-dimensional nature of the interdigitated flowfield.

Assuming single-phase transport in PEM fuel cells, a number of 3D models have been published. Notable ones include Dutta et al. [8], Um and Wang [9], and Zhou and Liu [10]. The present model features a single-domain formulation without requiring boundary conditions at interfaces internal to the fuel cell, thus facilitating implementation into a commercial computational fluid dynamics (CFD) package. In addition, the model contains a detailed membrane–electrode assembly (MEA) submodel where the water content distribution within the membrane and spatial variations of reaction rate and ionic resistance within the catalyst layer are fully resolved.

In the present work, the CFCD model developed by Um et al. [1] is extended to study electrochemical kinetics, current distribution, fuel and oxidant flow, and multi-component transport in a PEM fuel cell with both a straight and an interdigitated air cathode. Fully three-dimensional computations are performed, and results of the flowfield, species profiles and current density distribution are presented with emphasis on the air cathode. Polarization curves for conventional and interdigitated flowfields are simulated and compared.

2. Numerical model

Fig. 1 schematically shows a PEM fuel cell and its various components: the anode gas channel, gas-diffusion anode, anode catalyst layer, ionomeric membrane, cathode catalyst layer, gas-diffusion cathode, and an interdigitated cathode flow channel. Dry air is fed into the cathode channel, whereas humidified hydrogen is supplied to the anode channel. Hydrogen oxidation and oxygen reduction reactions are considered to occur only within the active catalyst layers where Pt/C catalysts are intermixed uniformly with recast ionomer.

The fuel and oxidant flow rates can be described by a stoichiometric flow ratio, ζ, defined as the amount of reactant in the chamber gas feed divided by the amount required by the electrochemical reaction. That is,

$$\zeta_c = X_{O_2,in}\vartheta_{c,in}\frac{P_c}{RT}\frac{4F}{I_{ref}A} \quad (1)$$

$$\zeta_a = X_{H_2,in}\vartheta_{a,in}\frac{P_a}{RT}\frac{2F}{I_{ref}A} \quad (2)$$

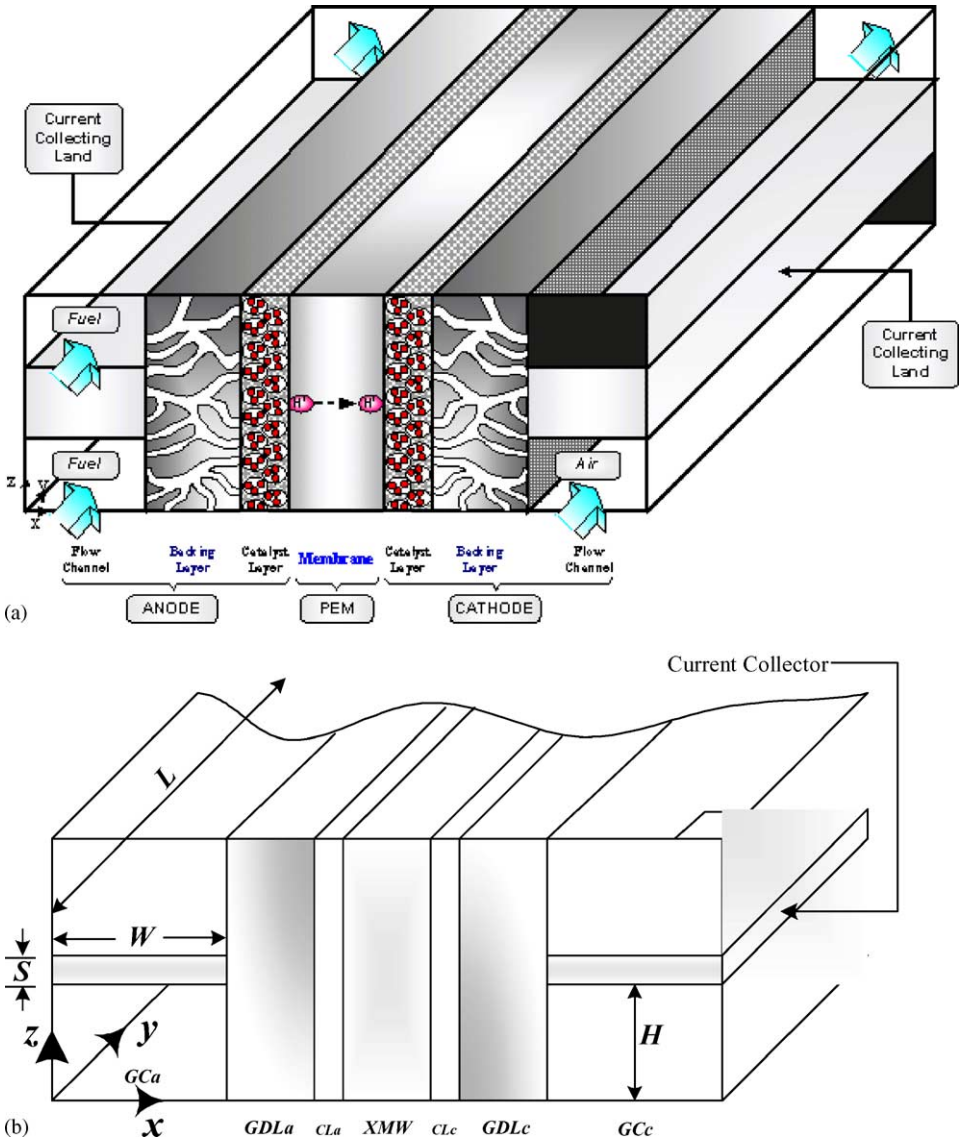

Fig. 1. (a) Three-dimensional schematic diagram and (b) geometrical description of a PEM fuel cell.

where ϑ is the inlet volumetric flow rate to a gas channel, P and T the pressure and temperature, R and F the universal gas constant and Faraday's constant, I_{ref} the current density, and A the electrode geometrical area. The subscripts 'c' and 'a' denote the cathode and anode sides, respectively. The stoichiometric flow ratios defined in Eqs. (1) and (2) are chosen to be based on a fixed reference current density of 1 A/cm^2 in the present work. Thus, flow rates of the fuel and oxidant are constant.

2.1. Model assumptions

The present model assumes:

- ideal gas mixtures;
- incompressible and laminar flow due to small pressure gradients and Reynolds numbers;
- isotropic and homogeneous electrodes, catalyst layers and membrane;
- constant cell temperature;
- negligible ohmic drop in the electronically-conductive solid matrix of porous electrodes, catalyst layers, and the current collectors; and
- existence of liquid water in small volume fraction and as finely dispersed droplets (i.e. mist flow) so that it does not affect the gas flow, transport, and electrochemical processes. This single-phase assumption then allows for super-saturation of water in the gas phase, namely the water activity greater than unity [11].

2.2. Governing equations

The 3D flow and electrochemical simulations described in the following are based on the single-domain fuel cell model

Table 1
Source terms for momentum, species, and charge conservation equations in various regions of a polymer electrolyte fuel cell

	Source terms			
	Flow channels	GDL	Catalyst layers	Membrane
Momentum	$S_u = 0$	$S_u = -\frac{\mu}{K}\varepsilon^2\vec{u}$	$\vec{u} = 0$	$\vec{u} = 0$
Species	$S_k = 0$	$S_k = 0$	$S_k = -\nabla\cdot\left(\frac{n_d}{F}I_e\right) - \frac{s_k j}{nF}$	$S_k = -\nabla\cdot\left(\frac{n_d}{F}I_e\right)$
Charge	$S_\Phi = 0$	$S_\Phi = 0$	$S_\Phi = j$	$S_\Phi = 0$

developed by Um et al. [1]. The model consists of non-linear, coupled partial differential equations representing the conservation of mass, momentum, species, and charge with electrochemical reactions.

The conservation equations are written in the vector form, as [1]

$$\frac{\partial(\varepsilon\rho)}{\partial t} + \nabla\cdot(\varepsilon\rho\vec{u}) = 0, \tag{3}$$

$$\frac{\partial(\varepsilon\rho\vec{u})}{\partial t} + \nabla\cdot(\varepsilon\rho\vec{u}\vec{u}) = -\varepsilon\nabla P + \nabla\cdot(\varepsilon\mu^{\text{eff}}\nabla\vec{u}) + S_u, \tag{4}$$

$$\frac{\partial(\varepsilon c_k)}{\partial t} + \nabla\cdot(\varepsilon\vec{u}c_k) = \nabla\cdot(D_k^{\text{eff}}\nabla c_k) + S_k, \tag{5}$$

$$\nabla\cdot(\kappa_e^{\text{eff}}\nabla\Phi_e) + S_\Phi = 0 \tag{6}$$

where $\vec{u}$, p, c_k, and Φ_e denote the intrinsic fluid velocity vector, pressure, molar concentration of chemical species k, and the phase potential of the electrolyte membrane, respectively. Details of the various source terms are summarized in Table 1.

The local current density in the mid-section of the membrane can be calculated as follows:

$$I(y,z) = -\kappa_e^{\text{eff}}\left.\frac{\partial\Phi}{\partial x}\right|_{x=\text{M.M.}} \tag{7}$$

where subscript M.M. represents the mid-section in the membrane. The average current density is then determined from

$$I_{\text{avg}} = \frac{1}{A}\int_A (y,z)\,\mathrm{d}A \tag{8}$$

where A is the electrode geometrical area.

2.3. Boundary conditions

Eqs. (3)–(6) form a complete set of governing equations for $(m + 5)$ unknowns where m is the physical dimension of the problem: $\vec{u}$, P, c_{H_2}, c_{O_2}, c_{H_2O}, and Φ_e. Due to the single-domain formulation, boundary conditions are required only at the external surfaces of the computational domain. At the fuel and oxidant inlets, the following conditions are prescribed:

$$\begin{aligned} &u_{\text{in,anode}} = U_{\text{a,in}}, u_{\text{in,cathode}} = U_{\text{c,in}};\\ &c_{H_2,\text{anode}} = c_{H_2,\text{a}}, c_{O_2,\text{cathode}} = c_{O_2,\text{c}}, c_{H_2O,\text{anode}}\\ &\quad = c_{H_2O,\text{a}}, c_{H_2O,\text{cathode}} = c_{H_2O,\text{c}} \end{aligned} \tag{9}$$

The inlet velocities of fuel and oxidant can also be expressed by their respective stoichiometric flow ratios, i.e. ζ_a and ζ_c at the fixed reference current density of 1 A/cm^2. At

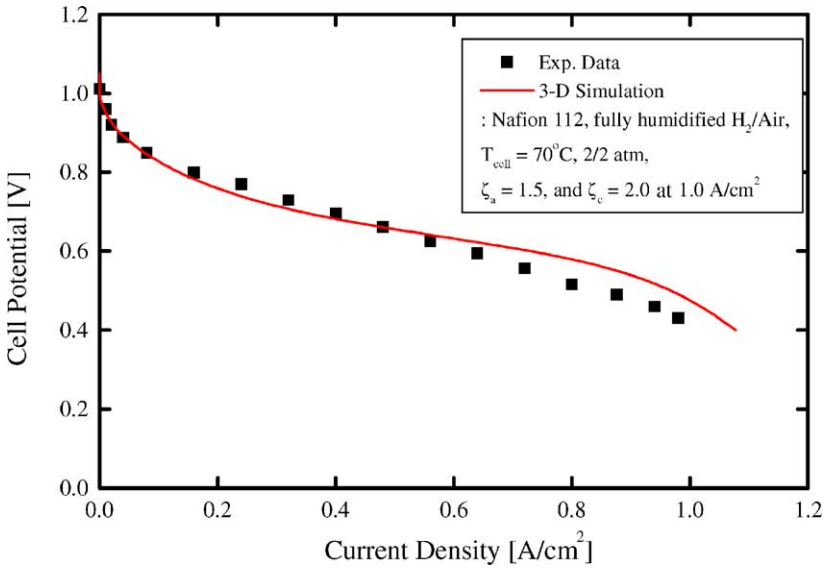

Fig. 2. Comparison of three-dimensional simulation with an experimental polarization curve.

Table 2
Electrochemical kinetics

Description	Anode	Cathode
Open circuit potential [16], V_{oc} (V)	$V_{a,oc} = 0$	$V_{c,oc} = 0.0025T + 0.2329$
Exchange current density times reaction surface area, aj_0^{ref} (A/m^3)	1.0×10^9	$3 \times 10^5 \exp[0.014189(T - 353)]$
Transfer coefficient, α	$\alpha_a + \alpha_c = 2$	$\alpha_c = 1$
Faraday constant, F (C/eq.)		96487

Table 3
Transport properties

Property	Value	Reference
Ionic conductivity of membrane, κ (S/m)	$(0.5139\lambda - 0.326)\exp\left[1268\left(\frac{1}{303} - \frac{1}{T}\right)\right]$	Springer et al. [11]
Electro-osmotic drag coefficient, n_d	1	Zawodzinski et al. [17]
H_2O diffusion coefficient in membrane, D_W^m (m^2/s)	$D_W^m = \begin{cases} 3.1 \times 10^{-7}\lambda(e^{0.28\lambda} - 1)\, e^{(-2346/T)}, & \text{for } 0 < \lambda \le 3 \\ 4.17 \times 10^{-8}\lambda(1 + 161\, e^{-\lambda})\, e^{(-2346/T)}, & \text{otherwise} \end{cases}$	Yeo and Eisenberg [18]
H_2 diffusivity in gas, D_{H_2} (m^2/s)	$1.1 \times 10^{-4}\left(\frac{T}{353}\right)^{3/2}\left(\frac{1}{P}\right)$	Perry et al. [19]
O_2 diffusivity in gas, D_{O_2} (m^2/s)	$3.2 \times 10^{-5}\left(\frac{T}{353}\right)^{3/2}\left(\frac{1}{P}\right)$	Perry et al. [19]
H_2 diffusivity in membrane, $D_{H_2}^m$ (m^2/s)	2.59×10^{-10}	Bernardi and Verbrugge [20]
O_2 diffusivity in membrane, $D_{O_2}^m$ (m^2/s)	1.22×10^{-10}	Bernardi and Verbrugge [20]
H_2O diffusivity in gas, D_{H_2O} (m^2/s)	$7.35 \times 10^{-5}\left(\frac{T}{353}\right)^{3/2}\left(\frac{1}{P}\right)$	Perry et al. [19]

the outlets, both anode and cathode channels assumed sufficiently long so that velocity and species concentration fields are fully developed.

2.4. Numerical procedures

The conservation equations, Eqs. (3)–(6), were discretized using a finite volume method [12] and solved using a general-purpose computational fluid dynamic code. Details of the numerical solution procedure and the code have been given in previous work [1]. It should be mentioned that although some species are practically non-existing in certain regions of a fuel cell, the species transport equation can still be applied throughout the entire computational domain by using the large source term technique originally proposed by Voller [13]. For instance, no hydrogen virtually exists in the cathode side of the computational domain in which a sufficiently large source term is assigned to the hydrogen transport equation, freezing the hydrogen mole fraction at zero.

Stringent numerical tests were performed to ensure that the solutions were independent of the grid size. A $39 \times 100 \times 40$ mesh (or, about 160,000 grid points) was found to provide sufficient spatial resolution. The coupled set of equations was solved iteratively, and the solution was considered to be convergent when the relative error in each field between two consecutive iterations was less than 10^{-5}.

Table 4
Cell design parameters

Description	Symbol	Value
Cell/electrode length (cm)	L	7.112
Gas channel height (cm)	H	0.0762
Gas channel width (cm)	W	0.0762
Current-collector width (cm)	$S\ (= \frac{1}{4}H)$	0.01905
Anode GDL thickness (cm)	GDL_a	0.0254
Porosity of anode GDL	ε_a	0.4
Anode catalyst layer thickness (cm)	CL_a	0.001
Porosity of anode catalyst layer	ε_{CL_a}	0.112
Membrane thickness (Nafion 117) (cm)	XMW	0.0178
Cathode catalyst layer thickness (cm)	CL_c	0.001
Porosity of cathode catalyst layer	ε_{CLc}	0.112
Porosity of cathode GDL	ε_c	0.4
Cathode GDL thickness (cm)	GDL_c	0.0254

Table 5
Cell operating conditions

Description	Symbol	Value
Cell temperature (°C)	T_{cell}	80
Pressure at the anode gas channel inlet (atm)	P_a	1.5
Relative humidity of inlet fuel stream (%)	RH_a	100
Reference current density (A/cm^2)	I_{ref}	1
Anode stoichiometry	ζ_a	1.5
Pressure at the cathode gas channel inlet (atm)	P_c	1.5
Relative humidity of inlet air stream (%)	RH_c	0
Cathode stoichiometry	ζ_c	1.8
Inlet nitrogen–oxygen mole fraction ratio	$X^c_{N_2,in}/X^c_{O_2,in}$	0.79/0.21

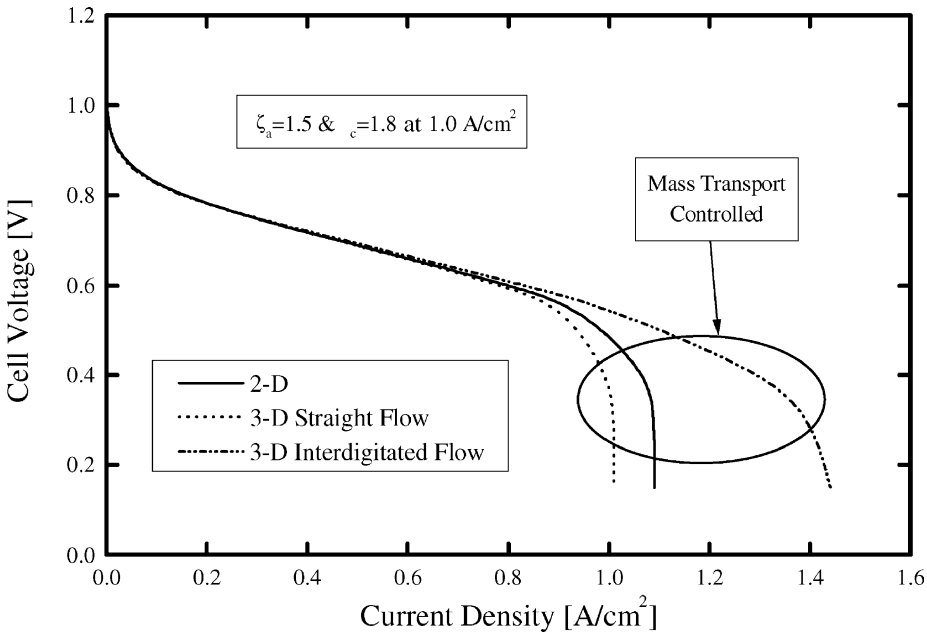

Fig. 3. Various polarization curves at $T_{cell} = 80\,^{\circ}C$, and the anode/cathode stoichiometry of 1.5 and 1.8 at 1.0 A/cm^2.

3. Results and discussion

In addition to the validation process in the previous study [1], a set of experimental polarization data measured at Penn State Electrochemical Engine Center (ECEC) is compared to the present three-dimensional CFCD model. The present model predicts very close results to the experimental data as shown in Fig. 2.

Fig. 1 schematically shows the cell domain in this three-dimensional study. The geometry consisting of a pair of channels is unit cell allowing for both straight flow and interdigitated flowfields to be studied by simply changing the flow inlet and outlet locations on the cathode side. The physical and transport properties as well as the electrochemical kinetics used in the present work are summarized in Tables 2 and 3.

A Nafion 117 membrane is chosen for the following computational study because this membrane has been used in the majority of prior modeling works [11,14,15]. Important geometrical parameters are listed in Table 4 and schematically shown in Fig. 1(b) for clarity. Cell operating conditions are given in Table 5.

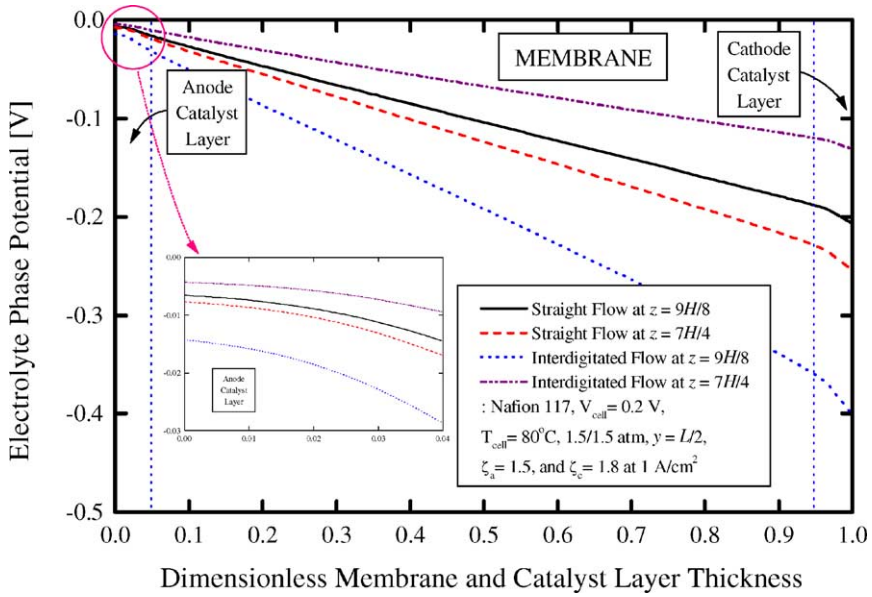

Fig. 4. Interdigitated effect on the electrolyte potential field at $V_{cell} = 0.2$ V.

3.1. Comparison of polarization curves

Fig. 3 shows the effect of the interdigitated flowfield on the cell performance. There is little difference in the current densities between a conventional and an interdigitated cathode until the cell voltage of 0.6 V, because the cell polarization for current densities below 0.8 A/cm^2 is dominated by cathode kinetic polarization and ohmic resistance through the membrane. For I_{cell} >0.8 A/cm^2, the cell polarization curve begins to be limited by mass transport within the air cathode. In this range, the positive role of the interdigitated flowfield becomes apparent. It is seen that the interdigitated flowfield improves the local current density by 40% at $V_{cell} = 0.3$ V, compared to that of the straight design, a result of enhanced mass transfer of oxidizer to the catalyst layer. Fig. 3 also displays a polarization curve generated by the two-dimensional model that does not take the rib effect into account. The two-dimensional simulation overpredicts the current density, because the landing area obstructing the gas transport is neglected.

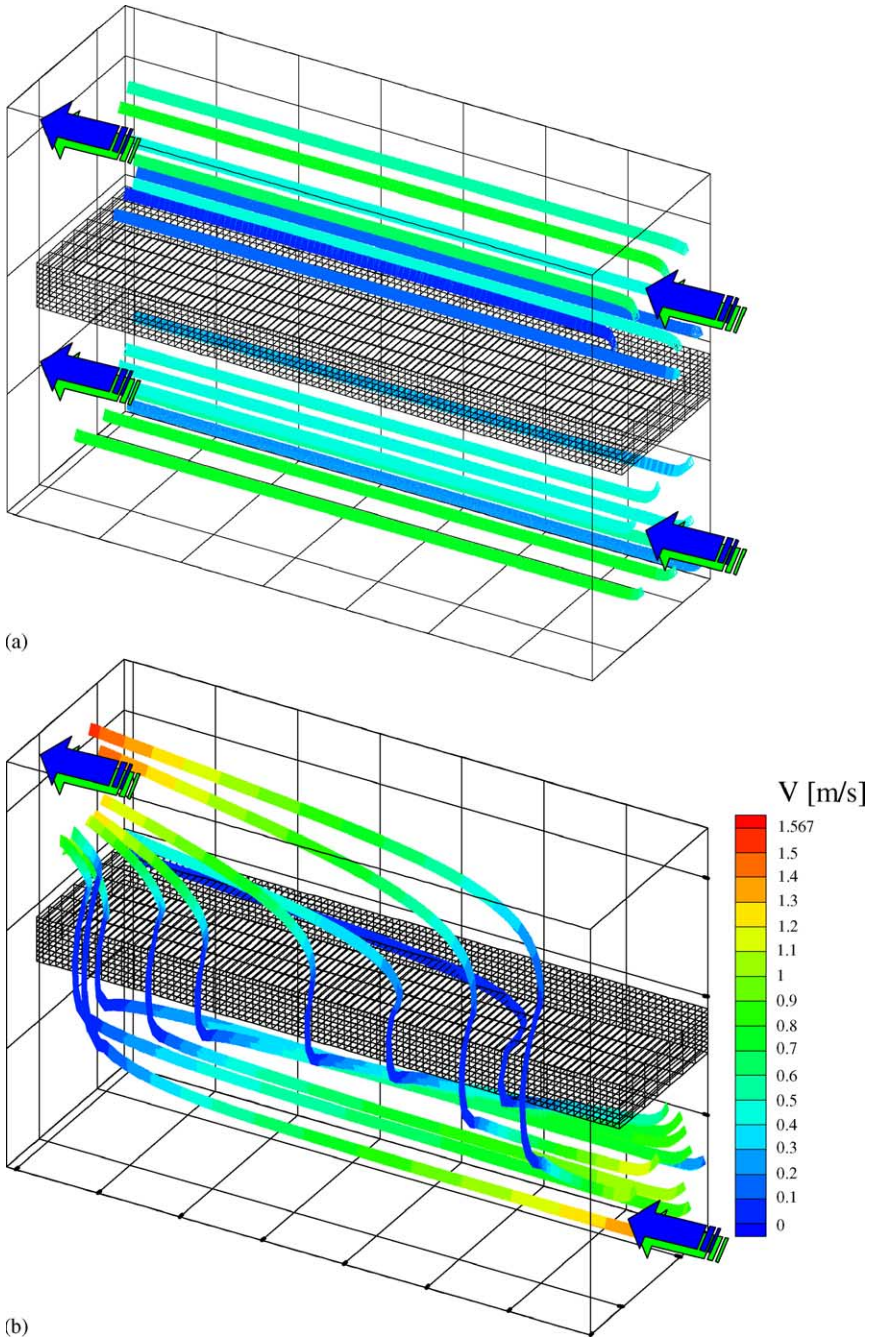

Fig. 5. Flow streamtraces across the cathode gas channel and GDL: (a) straight flow and (b) interdigitated flow at $V_{cell} = 0.2$ V.

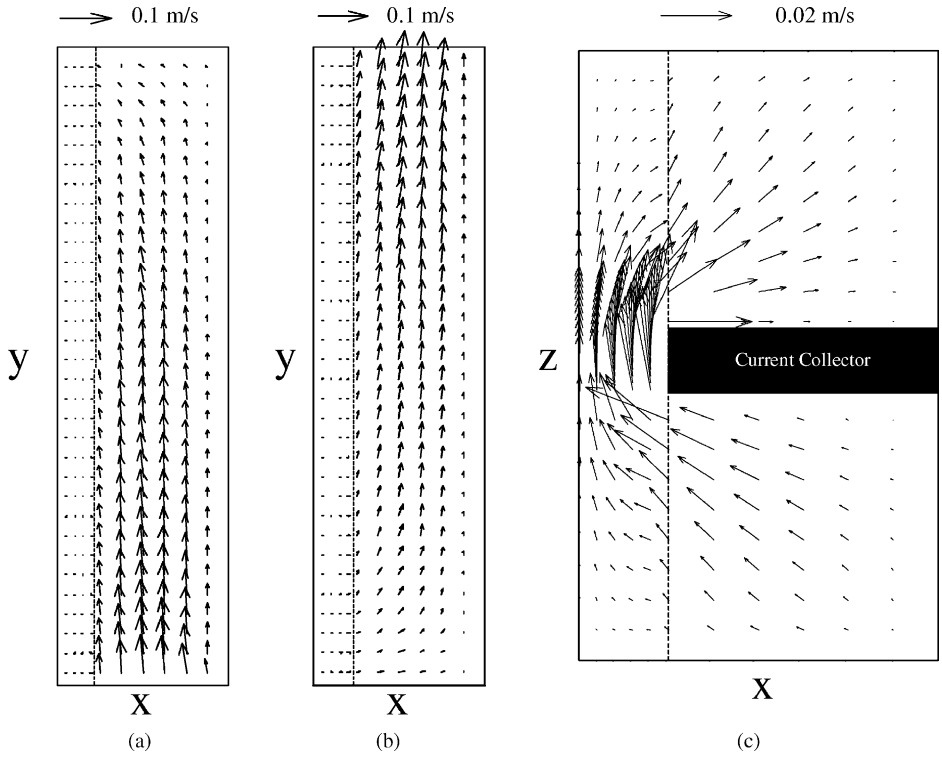

Fig. 6. Velocity profiles in the interdigitated flowfield: (a) on the x–y plane in the lower channel at $z = H/2$; (b) on the x–y plane in the upper channel at $z = 7H/4$; and (c) on the x–z plane at $y = L/2$. The cell operating conditions are the same as in Figs. 4 and 5.

3.2. Membrane potential distribution

Predicted electrolyte phase potential profiles across the membrane and the anode and cathode catalyst layers are illustrated in Fig. 4 for the mid-plane of the land (i.e. $z = (9/8)H$) and the half-plane of the upper channel ($z = (7/4)H$), respectively. It is seen that the slope of the potential profile (i.e. the current density) greatly increases in the area under the land ($z = (9/8)H$) in the interdigitated design due primarily to the enhanced oxygen supply by forced convection. However, the potential curve slope in the area under the upper exiting channel ($z = (7/4)H$)

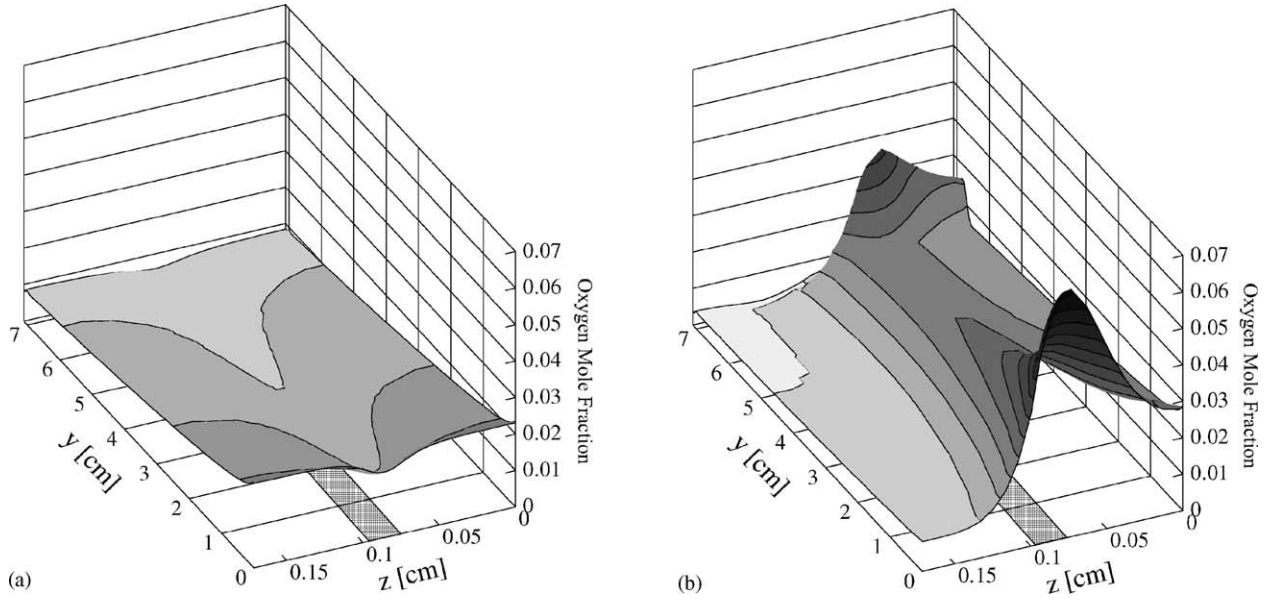

Fig. 7. Oxygen mole fraction distributions on y–z plane at the cathode reaction surface: (a) straight flow and (b) interdigitated flow at $V_{cell} = 0.2$ V. The shaded area is underneath the current-collecting land.

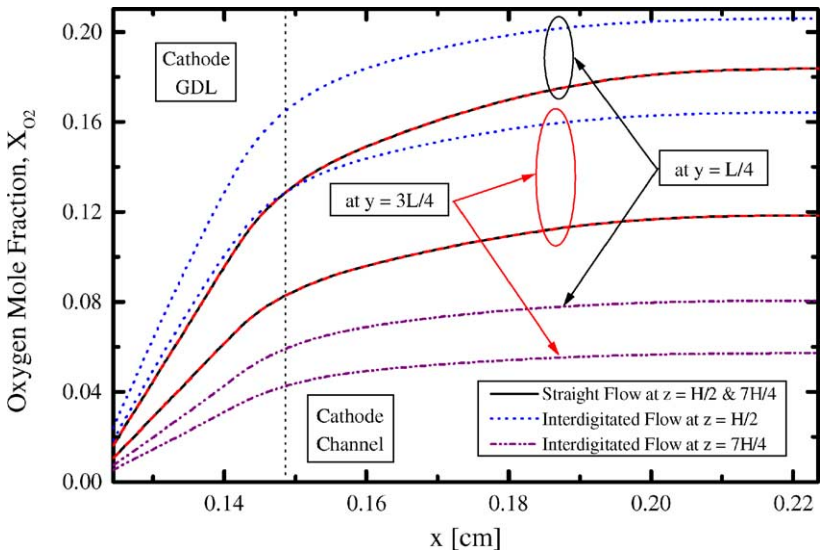

Fig. 8. Local profiles of oxygen mole fraction along x-direction at $V_{cell} = 0.2$ V.

becomes smaller in the interdigitated design than the straight channel design due to more depleted oxygen.

3.3. Flowfield

Fig. 5 shows the predicted flowfields within the porous cathode and its adjacent flow channels for conventional and interdigitated flowfields, respectively. Fig. 5(a) shows straight streamtraces in the conventional flow channel. In contrast, the streamtraces shown in Fig. 5(b) for interdigitated flow channels indicate that air comes in along the lower channel, penetrates through the porous GDL, merges, and exits through the upper channel. During this process, oxygen is brought to the cathode catalyst reaction site by forced convection rather than by diffusion as in the conventional design. Forced convection also enhances water removal compared to the conventional design. As a result, flooding of the cathode GDL is likely less severe, and better cell performance in the mass-transport control regime may be achieved with the interdigitated flowfield design.

Fig. 6 illustrates 2D vector plots in three representative planes of the cathode GDL and flow channel for the interdigitated flowfield. Fig. 6(a) corresponds to the mid-plane of the lower channel. It can be seen that the velocity is maximum at the inlet and gradually diminishes along the flow channel until reaching zero at the far end. The velocity scale within the GDL (separated by a dashed line) is several orders of magnitude smaller than that in the open channel and, thus, cannot be clearly displayed in Fig. 6(a). Fig. 6(b) illustrates the flowfield in the mid-plane of the upper channel. The front end of the channel is closed and thus has a zero velocity. But the fluid is continually supplied from the GDL and thus the flow velocity increases along the axial direction. The bypass flow around the current-collecting land is evident from the velocity field on the x–z plane at $y = L/2$ (the mid cross-section of the fuel cell) displayed in Fig. 6(c). This graph is also indicative of strong forced convection along the reaction surface (on the far left of the figure).

3.4. Concentration fields

Fig. 7 shows the oxygen mole fraction distribution on the y–z plane at the cathode reaction surface for both conventional and interdigitated air cathodes. The oxygen contour in the conventional straight channel decreases monotonically along the gas channel direction as the electrochemical reaction proceeds. For the interdigitated flow, however, the oxygen mole fraction becomes larger in the region underneath

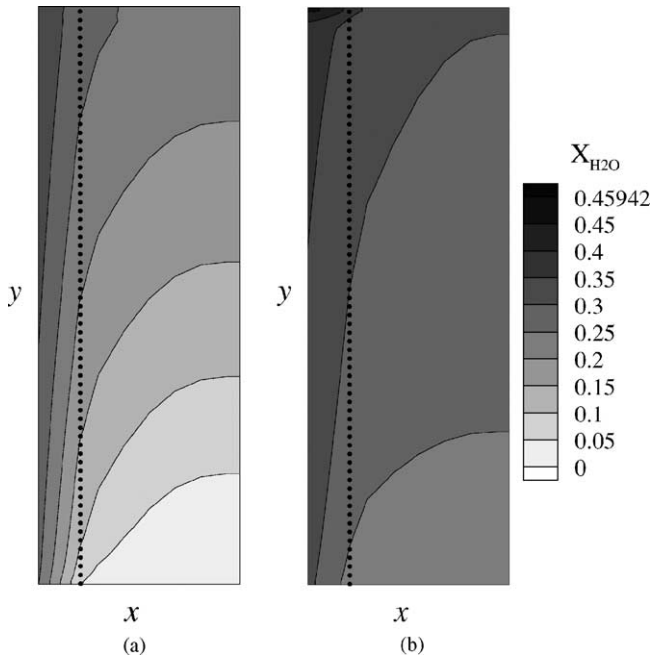

Fig. 9. Water vapor mole fraction contours on the x–y plane at $z = 7H/4$: (a) straight flow and (b) interdigitated flow at $V_{cell} = 0.2$ V.

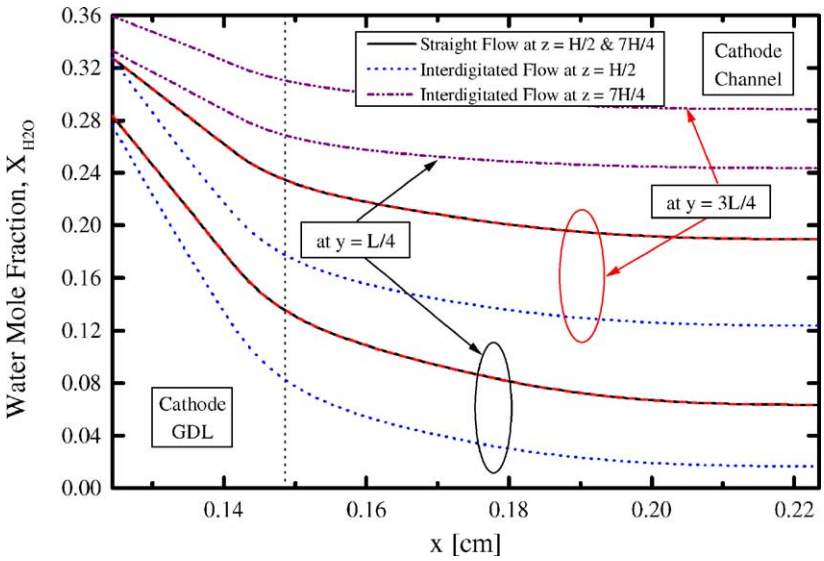

Fig. 10. Local profiles of water vapor mole fraction along x-direction at $V_{cell} = 0.2$ V.

the current-collector rib due to enhanced transport by forced convection. Notice that the current density distributions (to be shown in Fig. 11) closely follow those of the oxygen mole fraction shown in Fig. 7.

Fig. 8 displays the predicted local oxygen mole fraction profiles in the GDL and its neighboring gas channel at two selected axial locations. In the conventional flowfield, the oxygen distributions in the lower and upper channels are symmetric, and the concentration gradients occur only in the x-direction. However, in the interdigitated flowfield, the oxygen concentration profile becomes asymmetric in the z-direction. On average, the oxygen mole fraction on the cathode reaction surface under the inlet channel ($z = H/2$) is higher in the interdigitated flowfield than in the conventional flowfield, despite a steeper gradient across the GDL resulting from the higher current density. But this trend reverses in the catalyst layer under the exiting channel ($z = (7/4)H$) due to more depletion of oxygen in the upstream. In addition, interdigitated flow produces the larger oxygen mole fraction in the inlet channel than that in the conventional straight design, while this is reversed in the exit channel as shown in Fig. 8. As seen from Fig. 6(c), forced convection induced by the interdigitated design carries most of oxygen to the catalytic reaction area under the land, which is an ineffective zone in the conventional straight design due to slow diffusion of the oxidant.

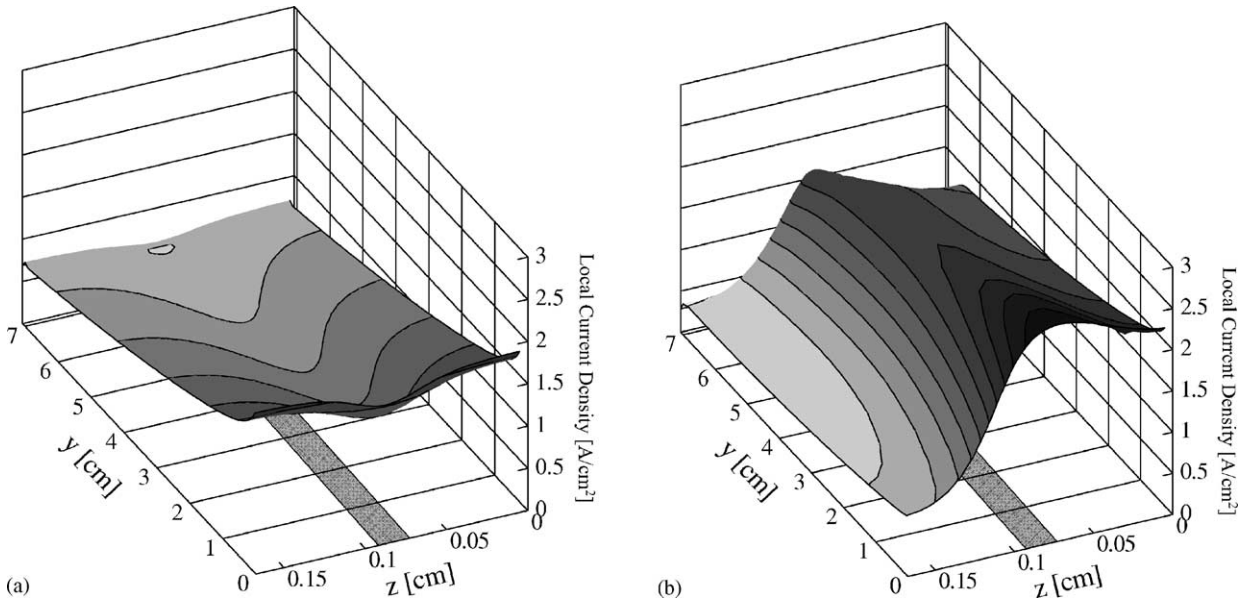

Fig. 11. Local current density distributions on y–z plane at the cathode reaction surface: (a) straight flow and (b) interdigitated flow at $V_{cell} = 0.2$ V. The shaded area is underneath the current-collecting land.

In the interdigitated flowfield, however, production of water vapor is greatly increased by the enhanced reaction rate. Fig. 9 displays the water mole fraction contours in straight and interdigitated flow, respectively. Note that the maximum mole fractions of water vapor in both cases exceed the saturated value ($X^{sat}_{H_2O} = 0.3118$ at a cell temperature of 80 °C and 1.5 atm), indicating that vapor condensation takes place. But condensation is confined to a very small region. Also the resulting volume fraction of liquid water can be expected very small. Thus, the present simulations shown in Fig. 9 can still be considered a good approximation. For more accurate predictions, a two-phase flow analysis is warranted where cell current densities are high. Fig. 9 displays the water vapor mole fraction distributions along the axial direction of the fuel cell on the x–y plane at $z = 7H/4$. Clearly, the exit stream contains much more water vapor in the interdigitated design (Fig. 9(b)) than that in the conventional design (Fig. 9(a)).

Fig. 10 displays the predicted local water vapor mole fraction profiles in the cathode GDL and its neighboring gas channel at two selected axial locations, i.e. $y = L/4$ and $(3/4)L$. Interdigitated flow predicts the higher water vapor mole fraction in the exit channel than that in the conventional straight design and vice versa in the inlet channel.

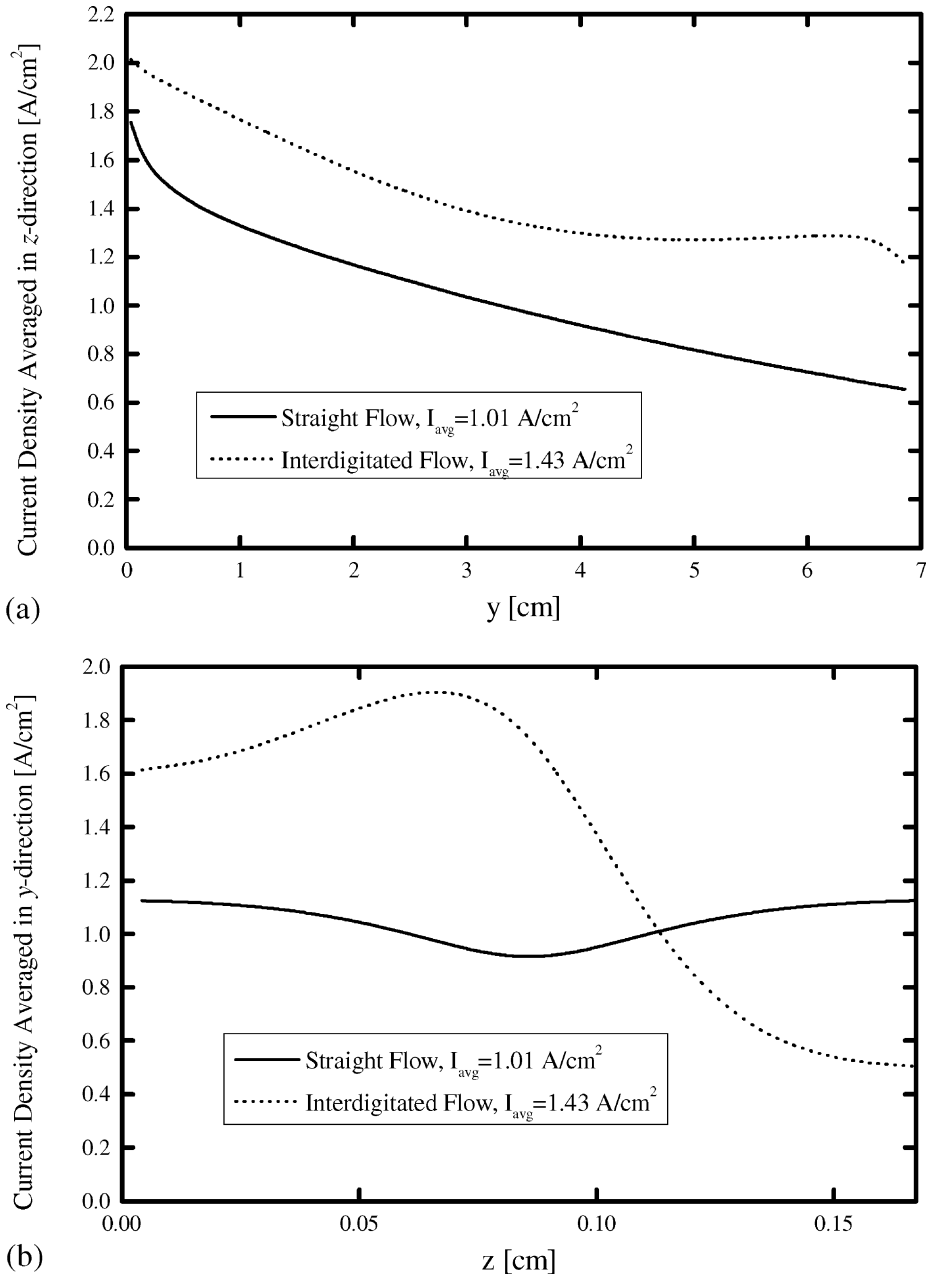

Fig. 12. Current density profiles averaged in: (a) z-direction and (b) y-direction at $V_{cell} = 0.2$ V.

The different characteristics of water distribution is a direct result of the altered flow structure between straight and interdigitated designs.

3.5. Current distribution

Fig. 11 depicts the current distribution on the reaction surface (on the *y*–*z* plane). For the conventional flowfield, the current density contours are symmetric about the centerline of the current-collector rib with the minimum located in the region under the rib. Along the flow direction (i.e. *y*-direction), the local current density decreases as the oxygen concentration is reduced. In the interdigitated flowfield, the local current density is very high near the entrance of the inlet channel because the oxygen concentration is the highest. This is followed by decreasing current density along the flow channel direction, due to the reduced oxygen concentration. Figs. 11(a) and (b) sharply contrast the current density distributions in the region underneath the current-collecting land between the conventional and interdigitated flowfields. As shown in Fig. 11(b), the mass-transport limitation in the area under the land can be greatly relaxed by forced convection induced by the interdigitated design.

Current density profiles, averaged along the *y*- and *z*-directions, respectively, are illustrated in Fig. 12 for $V_{\text{cell}} = 0.2\,\text{V}$. The effect of interdigitated flow on the current density is evident over the entire cell length at this low cell voltage (or high average current density). The local current density generally decreases along the *y*-direction toward the channel end, as the oxidant supply is gradually depleted as shown in Fig. 12(a). Fig. 12(b) illustrates the local current density profile along the *z*-direction. For the conventional straight flow design, current density is symmetric about the centerline where the minimum current density appears in the area under the land, due to the larger mass-transport resistance there. In contrast, in the interdigitated flow, the maximum current density exists in the region underneath the land due to the forced convection through the porous GDL. Also, most of available oxygen is consumed in the upstream (i.e. the areas under the inlet channel and land) in the interdigitated design, leaving lower local current density in the catalyst layer under the exit channel (i.e. the downstream). Most importantly, it is noted that although the interdigitated flow creates a higher average current density than the straight flow, its current distribution is also much more non-uniform.

4. Conclusions

A three-dimensional computational model has been applied to predict the fuel cell performance with both the conventional and interdigitated cathode flowfields. The effects of the interdigitated flowfield on oxygen transport and water removal are illustrated through three-dimensional results of the flow structure, oxygen and water concentration distributions. It is shown that there exist profound interactions between the flowfield and the current and species distribution in PEM fuel cells. The fully three-dimensional model of electrochemical reactions, current distribution, gas dynamics and multi-component transport as presented herein is shown to be able to: (1) understand the many interacting, complex electrochemical and transport phenomena that cannot be studied experimentally; (2) identify limiting steps and components; and (3) provide a computer-aided tool for design and optimization of future fuel cell engines with much higher power density and lower cost.

A detailed study of water transport throughout a PEM fuel cell under low-humidity operation using the same single-domain model will be presented in a separate publication.

Acknowledgements

This work is supported by NSF under grants nos. DUE-9979579 and CTS-9733662, US Department of Energy under the Ultra-Clean Fuel Program, and Delphi Automotive Systems.

References

[1] S. Um, C.Y. Wang, K.S. Chen, J. Electrochem. Soc. 147 (2000) 4485.
[2] M.S. Wilson, F.H. Garzon, K.E. Sickafus, S. Gottesfeld, J. Electrochem. Soc. 140 (1993) 2872.
[3] T.V. Nguyen, J. Electrochem. Soc. 143 (1996) L103.
[4] D.L. Wood, J.S. Yi, T.V. Nguyen, Electrochim. Acta 43 (1998) 3795.
[5] W. He, J.S. Yi, T.V. Nguyen, AIChE J. 46 (2000) 2053.
[6] J.S. Yi, T.V. Nguyen, J. Electrochem. Soc. 146 (1999) 38.
[7] A. Kazim, H.T. Liu, P. Forges, J. Appl. Electrochem. 29 (1999) 1409.
[8] S. Dutta, S. Shimpalee, J.W. Van Zee, J. Appl. Electrochem. 30 (2000) 135.
[9] S. Um, C.Y. Wang, in: Proceedings of the Conference of IMECE, vol. 1, Orlando, FL, 2000, p. 19.
[10] T. Zhou, H. Liu, Int. J. Transport Phenom. 3 (2001) 177.
[11] T.E. Springer, T.A. Zawodinski, S. Gottesfeld, J. Electrochem. Soc. 136 (1991) 334.
[12] S.V. Patankar, Numerical Heat Transfer and Fluid Flow, Hemisphere, New York, 1980.
[13] V.R. Voller, Num. Heat Transfer, Part B 17 (1990) 155.
[14] T.E. Springer, M.S. Wilson, S. Gottesfeld, J. Electrochem. Soc. 140 (1993) 3513.
[15] T.E. Springer, T. Rockward, T.A. Zawodzinski, S. Gottesfeld, J. Electrochem. Soc. 148 (2001) A11.
[16] A. Parthasarathy, S. Srinivasan, A.J. Appleby, J. Electrochem. Soc. 139 (1992) 2530.
[17] T.A. Zawodzinski, J. Davey, J. Valerio, S. Gottesfeld, Electrochim. Acta 40 (1995) 297.
[18] S.W. Yeo, A. Eisenberg, J. Appl. Polym. Sci. 21 (1977) 875.
[19] R.H. Perry, D.W. Green, J.O. Maloney, Perry's Chemical Engineers' Handbook, McGraw-Hill, New York, 1984.
[20] D.M. Bernardi, M.W. Verbrugge, J. Electrochem. Soc. 139 (1992) 2477.